Signatures of Coronal Loop Opening via Interchange Reconnection in the Slow Solar Wind at 1 AU

Mathew Owens[1] · Mike Lockwood[1] ·
Allan Macneil[1] · David Stansby[2]

Abstract The opening of closed magnetic loops via reconnection with open solar flux, so called "interchange reconnection", is invoked in a number of models of slow solar wind release. In the heliosphere, this is expected to result in local switchbacks or inversions in heliospheric magnetic flux (HMF). When observed at 1 AU, inverted HMF has previously been shown to exhibit high ion charge states, suggestive of hot coronal loops, and to map to the locations of coronal magnetic separatrices. However, simulations show that inverted HMF produced directly by reconnection in the low corona is unlikely to survive to 1 AU without the amplification by solar wind speed shear. By considering the surrounding solar wind, we show that inverted HMF is preferably associated with regions of solar wind shear at 1 AU. Compared with the surrounding solar wind, inverted HMF intervals have lower magnetic field intensity and show intermediate speed and density values between the faster, more tenuous wind ahead and the slower, denser wind behind. There is no coherent signature in iron charge states, but oxygen and carbon charge states within the inverted HMF are in agreement with the higher values in the slow wind behind. Conversely, the iron-to-oxygen abundance ratio is in better agreement with the lower values in the solar wind ahead, while the alpha-to-proton abundance ratio shows no variation. One possible explanation for these observations is that the interchange reconnection (and subsequent solar wind shear) that is responsible for generation of inverted HMF involves very small, quiet-Sun loops of approximately photospheric composition, which are impulsively heated in the low corona, rather than large-scale active region loops with enhanced first-ionisation potential elements. Whether signatures of such small loops could be detected in situ at 1 AU still remains to be determined.

Keywords Solar wind

✉ M. Owens
m.j.owens@reading.ac.uk

1   Department of Meteorology, University of Reading, Reading, UK

2   Mullard Space Science Laboratory, University College London, Holmbury St. Mary, Surrey,
     RH5 6NT, UK

1. Introduction

Fast solar wind originates in coronal holes that contain unipolar, open magnetic flux, while slow wind generally maps to the vicinity of closed loops within the streamer belt (e.g. Mc-Comas *et al.*, 2003). When observed in situ, fast wind exhibits lower plasma density and magnetic field intensity than slow wind, but higher plasma temperature (e.g. Ebert *et al.*, 2009). Ion charge states indicate that fast wind originates in cool coronal holes, while slow wind comes from hot coronal regions Geiss, Gloeckler, and von Steiger (1995). Similarly, ion abundance ratios in fast and slow wind are consistent with coronal holes and coronal loops, respectively von Steiger *et al.* (2000).

Plasma can readily escape from the low corona along open magnetic flux to become fast wind. But the association of slow wind with closed coronal loops makes the release of the source plasma more difficult to understand. One proposed solution is that the source of the slow wind is not the closed loops themselves, but the adjacent open flux which expands super-radially to drape over the loops, such as in the formation of helmet streamers (Newkirk, 1967). Combining potential-field source-surface (Schatten, Wilcox, and Ness, 1969) solutions of the observed photospheric magnetic field with in situ solar wind observations reveals a weak anti-correlation between the non-radial expansion of magnetic flux tubes and solar wind speed (Wang and Sheeley, 1990). The physical interpretation is that the over-expansion of the magnetic field causes the Alfvén speed to fall off rapidly with altitude and thus changes the height at which waves are reflected and damped (Cranmer, Ballegooijen, and Edgar, 2007). This, in turn, changes the proportions of wave energy which are converted to kinetic energy or thermal heating. As no change in magnetic topology is required for the release of the slow wind by this mechanism, this is often referred to as the steady-state solution.

The alternate class of solution involves time-dependent evolution of the magnetic field topology, which opens coronal loops via interchange reconnection with open flux (e.g. Crooker and Owens, 2011; Edmondson *et al.*, 2010). This process is observed to operate at the coronal hole boundary (Baker *et al.*, 2009) and is invoked to explain the rigid rotation of coronal magnetic fields despite the differential rotation of the photosphere (Nash, Sheeley, and Wang, 1988). It has also been proposed as a source of slow wind (Fisk, 2003). The network of small-scale magnetic separatrices expected to exist throughout the streamer belt (Antiochos *et al.*, 2011) means this process could potentially account for a substantial fraction of the observed slow wind. In the heliosphere, apparent periodicities observed within the solar wind in near-Earth space (Kepko *et al.*, 2016; Viall, Spence, and Kasper, 2009) are suggestive of time-dependent release processes. Such periodicities have also been observed remotely in the inner heliosphere, suggesting they originate from the corona.

Inversions or folds in heliospheric magnetic flux (HMF), sometimes referred to as "switchbacks", have long been observed in the fast wind on the basis of wave propagation and differential alpha-particle streaming direction (Balogh *et al.*, 1999; Yamauchi *et al.*, 2004). These structures have been associated with coronal plumes within the fast wind (Velli *et al.*, 2011). In both the fast and slow wind, suprathermal electron signatures can be used to identify the local inversions in HMF direction (Kahler, Crooker, and Gosling, 1996; Crooker *et al.*, 2004). Such HMF inversions could result from interchange reconnection between open flux and heliospheric closed loops (Crooker *et al.*, 2004) and have been linked with both coronal separatrices (Owens, Crooker, and Lockwood, 2013) and the latitudinal extent of the slow wind band (Owens, Crooker, and Lockwood, 2014).

Numerical magnetohydrodynamic (MHD) simulations of inverted HMF generated in the low corona suggest that it would rapidly decay and not survive to be observed in situ at
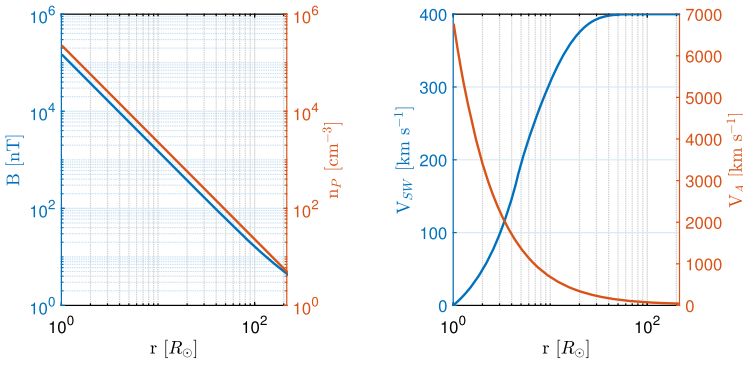
Figure 1 Variations of solar wind properties with heliocentric distance. Left: The blue line and axis show the heliospheric magnetic field intensity, B, obtained assuming corotation to 10 solar radii ($R_\odot$) and a perfect Parker spiral above that point with a 1-AU value of 4.5 nT. The orange line and axis show proton density, n_P, assuming constant mass flux and a 1-AU value of 5 cm^{-3}. Note the log scales on both axes. Right: The orange line and axis show the resulting Alfvén speed, V_A. The blue line and axis show the observationally constrained Parker solar wind profile, assuming a 1-AU value of 400 km s^{-1}. Note the log scale on the x axis only.

1 astronomical unit (AU) and beyond (Landi, Hellinger, and Velli, 2005, 2006). Instead, these authors propose that solar wind speed shear resulting from solar wind microstreams (Neugebauer *et al.*, 1995) could generate (and/or amplify) the HMF inversions during transit of the solar wind from the corona to 1 AU. Owens *et al.* (2018) proposed that solar wind shear is produced when the footpoint of the newly opened loop transitions from being a source of slow to fast wind. In the first part of this study, we use simple scaling arguments to demonstrate the principle of rapid decay of HMF inversions generated in the low corona and to investigate the effect of loop apex size at the time of interchange reconnection. This supports the previous findings that solar wind shear is necessary for inversions to survive to 1 AU. In the second part of the present study, we look at the association of inverted HMF with solar wind stream shear and coronal loop signatures in near-Earth in situ observations. While 1 AU is not ideal for such a study, as the solar wind has been highly processed and signatures of formation have likely been somewhat destroyed, we show there is an observable remnant. As such, these observations provide hints for the features that should be more readily identifiable in Parker Solar Probe (Fox *et al.*, 2016) and Solar Orbiter (Muller *et al.*, 2013) observations of the inner heliosphere.

2. Simple Model of Inverted HMF

Using a numerical MHD approach, Landi, Hellinger, and Velli (2005, 2006) have previously demonstrated that HMF inversions generated in the low corona would be unstable and decay within a few solar radii due to the magnetic curvature force. Owens *et al.* (2018) further argued that the sense of the initial solar wind speed shear resulting from interchange reconnection would be such to erode, rather than maintain, the inverted HMF. Here we use simple scaling arguments to illustrate the underlying reasons for expecting inverted HMF erosion due to the magnetic curvature force. Such simple order-of-magnitude computations are important for identifying the major and the minor contributors to an effect.
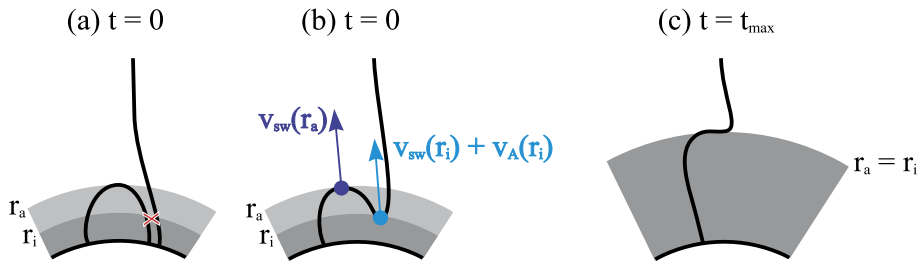
Figure 2 Schematic of the model used to estimate inverted HMF survival distance. (**a**) At time $t = 0$, interchange reconnection (red cross) between an open flux tube and a closed loop occurs at a height r_i. The closed loop has an apex height of r_a. (**b**) The loop apex begins to move at the local solar wind speed, $V_{SW}(r_a)$. The newly created inverted HMF moves at the local solar wind speed plus the local Alfvén speed, $V_{SW}(r_i) + V_A(r_i)$. The positions of the apex and loop are advanced numerically. (**c**) The inversion is assumed to survive until time t_{MAX}, when the inversion reaches the height of the loop apex, i.e. $r_a = r_i$.

It is first necessary to estimate the solar wind and Alfvén speeds as a function of heliocentric distance. By mass conservation, solar wind proton number density, n_P, must fall off as the inverse square of heliocentric distance, r. We take a 1-AU proton density of 5 cm^{-3} (typical of inverted HMF, as shown in Section 3) to compute the r profile shown as the orange line in Figure 1a. To compute the magnetic field intensity, B, variation with r, we assume the coronal magnetic field corotates with the Sun and falls off as $1/r^2$, while the heliospheric field is a perfect Parker spiral magnetic field, giving a radial fall off slower than $1/r^2$ owing to the azimuthal magnetic field component which is a function of solar wind speed and r. We use a 1-AU magnetic field intensity, B, of 4.5 nT (typical of inverted HMF, as demonstrated in Section 3). The transition between the coronal and heliospheric regimes is assumed to occur at 10 solar radii ($R_\odot$), approximately the Alfvén height, though varying this value between a typical source surface of 2.5 $R_\odot$ and a typical global corona model outer boundaries of 30 $R_\odot$ has very little effect on the results presented here. The resulting B profile is shown as the blue line in Figure 1a. B can be seen to fall off slightly slower than the $1/r^2$ variation of n_P, particularly past 100 $R_\odot$, as expected. Combining the B and n_P profiles gives the Alfvén speed, V_A, shown as the orange line in Figure 1b. Solar wind speed, V_{SW}, is assumed to follow a Parker-like solution (Parker, 1958), constrained by coronagraph (Sheeley *et al.*, 1997) and Doppler spectroscopic (Li *et al.*, 1998) observations. The resulting V_{SW} profile is shown as the blue line in Figure 1b. We take a 1-AU V_{SW} of 400 km s^{-1}. Using the given parameters and assumptions, at 1 AU we obtain $V_A = 45$ km s^{-1} and an Alfvén surface at 18 $R_\odot$.

As illustrated in Figure 2, inverted HMF is assumed to be produced at a time $t = 0$ by interchange reconnection of an open field line with a closed loop. At this time, the nadir of the resulting inversion is at a height r_i, while the apex of the loop is at a height r_a, where $r_a > r_i$ at $t = 0$. The apex propagates radially at the local solar wind speed, $V_{SW}(r_a)$, while the inversion propagates out at the local solar wind speed plus the local Alfvén speed, $V_{SW}(r_i) + V_A(r_i)$. Strictly speaking, in the solar wind frame the apex would also move sunwards at the local Alfvén speed, further reducing the inversion lifetime. However, given this one-dimensional approximation does not allow for the fact that only a component of V_A will act as the inversion flattens out, the effective factor 2 is omitted here. We compute the new positions and speeds of the apex and inversion at 10-second intervals. The inversion is defined to survive while $r_a > r_i$.

Figure 3 shows the inverted HMF survival height for a range of loop apex distances at $t = 0$. A reconnection height (and thus initial inverted HMF height) of 1.5 $R_\odot$ was used

Figure 3 The inverted HMF survival distance as a function of the loop apex at the time of interchange reconnection. The survival height (red) is estimated as the heliocentric distance at which the inverted HMF region, moving at the local Alfvén speed in the solar wind frame, catches up with the loop apex. The $y = x$ line is shown as the black dashed line.
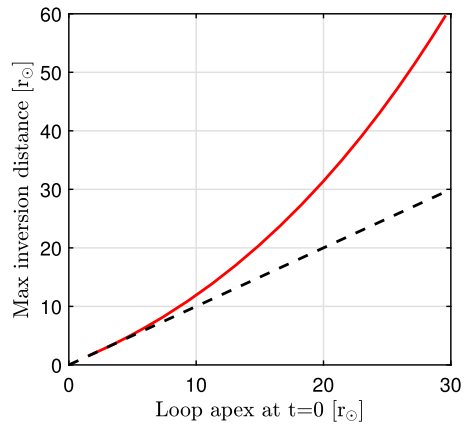

throughout. But high Alfvén speed in the low corona means essentially identical results were obtained for values between 1.05 and 2 $R_{\odot}$ (not shown). As with the far more physically complete MHD simulations (Landi, Hellinger, and Velli, 2005, 2006), the immediate conclusion is that non-eruptive coronal loops (which must have an apex height $\ll 20R_{\odot}$) do not directly produce inverted HMF which survives to 1 AU (i.e. 215 $R_{\odot}$) without additional amplification processes. We stress that this one-dimensional calculation is undoubtedly simplistic and a more accurate estimation of the inverted HMF survival height requires high spatial and temporal two- or three-dimensional magnetohydrodynamic (MHD) simulations. However, as the results are in broad agreement with Landi, Hellinger, and Velli (2005, 2006), due to similar scaling of solar wind parameters with distance, these results can still provide insight. We find that for the inverted HMF seen in near-Earth space to be the direct result of interchange reconnection, the loops must first erupt into the solar wind and travel a significant fraction of 1 AU before they are opened up by interchange reconnection. When encountered in situ, these loops would have an identifiable suprathermal electron signature (Gosling *et al.*, 1987). While this occurs for the closed magnetic flux contained in coronal mass ejections (Shodhan *et al.*, 2000; Riley, Gosling, and Crooker, 2004; Owens and Crooker, 2007), there is currently no observational evidence for the existence of a significant amount of closed HMF in the slow solar wind outside of CMEs. High quality suprathermal electron observations well inside 1 AU, such as provided by Parker Solar Probe and Solar Orbiter, may change this. However, at present, the most probable explanation for formation/amplification of inverted HMF is via dynamical solar wind speed shear processes in the heliosphere, either as a result of changing solar wind speed at the magnetic foot point (Lockwood, Owens, and Rouillard, 2009; Owens *et al.*, 2018; Landi, Hellinger, and Velli, 2005, 2006) or draping of the HMF in front of small-scale solar wind transients (Lockwood, Owens, and Macneil, 2019). In the next section, we investigate the association of inverted HMF with solar wind speed shear.

3. Observations of Inverted HMF

We now examine the solar wind context of inverted HMF at 1 AU. We follow the same procedure as Owens *et al.* (2018) and Owens *et al.* (2017) to identify individual inverted HMF intervals at 1 AU in 64-second Advanced Composition Explorer (ACE) magnetic field and suprathermal electron data (McComas *et al.*, 1998; Smith *et al.*, 1998). In brief, the

Figure 4 Cumulative
distribution functions of inverted
HMF interval durations (red) and
waiting time between consecutive
intervals (black).
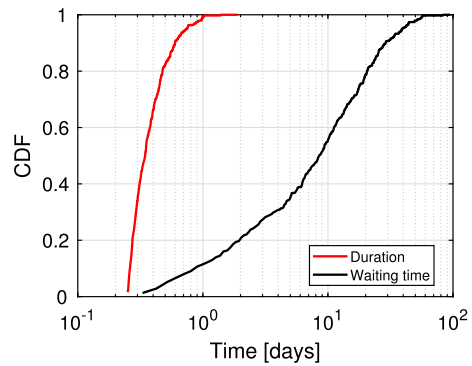
suprathermal electron beam, or "strahl" (Pilipp *et al.*, 1987), direction is identified in the 272 eV channel using a simple threshold approach. By comparison of the strahl and the HMF direction in the heliospheric frame, inverted HMF intervals are then defined relative to the heliocentric radial direction. Over the period 1 January 1998 to 1 June 2011 (the overlap with the available ion data, discussed below), this results in 281,388 64-second individual intervals of inverted HMF. Some of these are part of extended periods of inverted HMF, while others are short-lived, isolated changes in topology, likely the result of small-scale waves or turbulence.

Heavy ion data from the ACE/Solar Wind Ion Composition Spectrometer (SWICS) instrument (Gloeckler *et al.*, 1998) are available at 1-hour resolution as part of the "merged" dataset at ftp://cdaweb.gsfc.nasa.gov/pub/data/ace/multi. Thus we limit our analysis to only the longest-lived inverted HMF intervals. To identify these intervals, we begin by assigning each 64-second datum a topology flag 0 or 1 depending on whether it meets the sunward strahl criteria. We then apply a 3-hour running smooth to the topology flag time series, so as to mitigate the effect of longer inverted HMF intervals being split by a few 64-second measurements of uninverted HMF. We then apply a threshold of 0.5 to identify inverted HMF (i.e., intervals containing more inverted than uninverted HMF in a given period), taking the precise start/end times to be the first/last 64-second interval of inverted HMF for which the smoothed topology flag is at least 0.5. Finally, we take all inverted HMF intervals with a duration greater than 0.25 days. This results in 390 intervals for study. Clearly the choice of these thresholds is somewhat arbitrary, but the results presented here are not particularly sensitive to the exact values used.

We begin by considering the average properties of the inverted HMF intervals. Figure 4 shows the cumulative distribution function (CDFs) of the duration of inverted HMF intervals. The median duration is 8.3 hours, with an interquartile range of 6.8 to 10.8 hours. The maximum inverted HMF duration is just under 2 days. The waiting time between the end of one inverted HMF interval and the start of the next has a median value of 8.5 days and an interquartile range of 2.7 to 18.0 days.

We consider the pressure within an interval 2 days ahead of the leading inverted HMF boundary (P_{AHEAD}), 2 days after the trailing boundary (P_{INV}) and within the inverted HMF interval (P_{INV}). The fractional change in pressure from the ahead solar wind is given by $\Delta P = 2(P_{AHEAD} - P_{INV})/(P_{AHEAD} + P_{INV})$. Figure 5 shows the fractional change in magnetic, plasma, and total pressure across the leading and trailing HMF inversion boundaries. In general, there is a great deal of variability from event to event, with both increases and decreases in magnetic, plasma, and total pressure across the inverted HMF intervals. However, there are some notable trends. Both the plasma and magnetic pressures tend to be higher

Figure 5 The fractional change in magnetic (top), plasma (middle), and total (bottom) pressure. Red shows the fractional change in pressure between the 2-day interval ahead (P_{AHEAD}) and within the inversion (P_{INV}), i.e. $2(P_{AHEAD} - P_{INV})/(P_{AHEAD} + P_{INV})$. Blue shows the fractional change in pressure between the 2-day solar wind interval behind and within the inversion, i.e. $2(P_{BEHIND} - P_{INV})/(P_{BEHIND} + P_{INV})$.
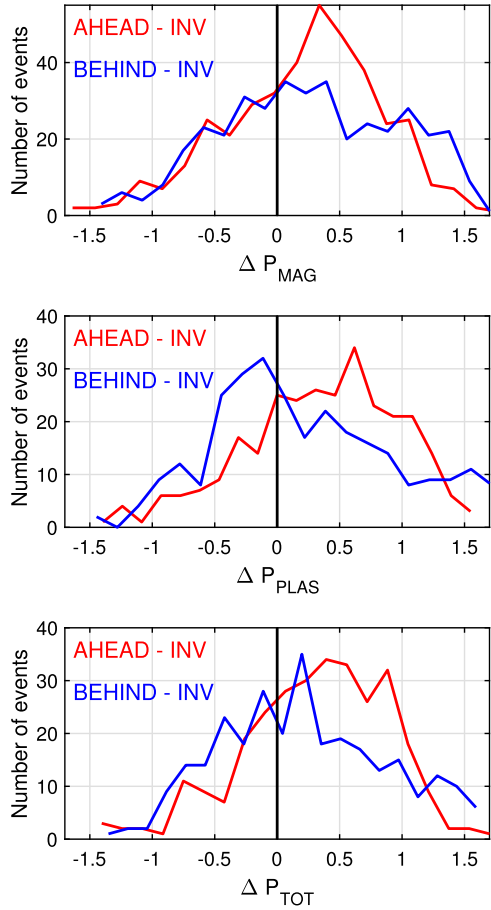
ahead of the inversion than inside. Thus the inverted HMF intervals are not generally in pressure balance with the solar wind ahead. With respect to the solar wind behind, however, the inverted HMF intervals have lower magnetic pressure, but higher plasma pressure, resulting in approximate pressure balance overall.

Previous studies of inverted HMF in the fast solar wind have reported structures that they are primarily Alfvénic in character, showing correlated magnetic field and velocity fluctuations (Balogh *et al.*, 1999; Horbury, Matteini, and Stansby, 2018; Matteini *et al.*, 2015). As will be demonstrated below, the inverted HMF considered here is largely associated with the slow solar wind. In order to quantify the Alfvénic nature (or otherwise) of inverted HMF intervals, we compute the cross helicity, σ_C, defined as (Bruno and Carbone, 2005; Stansby, Horbury, and Matteini, 2019):

$$\sigma_C = 2\frac{\langle \mathbf{v} \cdot \mathbf{b}\rangle}{\langle |\mathbf{v}|^2 + |\mathbf{b}|^2\rangle} \qquad (1)$$

where $\mathbf{v}$ is the proton velocity vector in the Alfvén wave frame and $\mathbf{b}$ is the magnetic field in velocity units (i.e., $\mathbf{b} = v_A \mathbf{B}/B$, where $\mathbf{B}$ is the magnetic field vector). As in Bruno and Carbone (2005) and Stansby, Horbury, and Matteini (2019), averages are taken over 20-
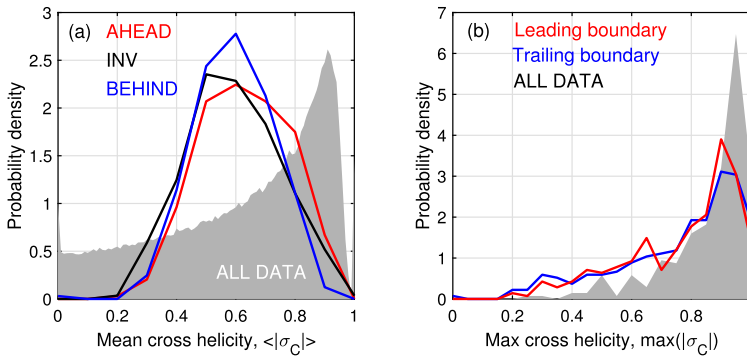
Figure 6 Probability densities of absolute cross helicity ($|\sigma_C|$) associated with inverted HMF. (**a**) Averaged over the whole ahead (red), behind (blue), and inverted HMF (black) intervals. The grey-shaded region shows the 8-hour mean across the whole dataset. (**b**) The maximum $|\sigma_C|$ in a 2-hour window centred on the leading (red) and trailing (blue) edge of the inverted HMF interval. The grey-shaded region shows the equivalent value for random periods within the same dataset.

minute intervals, with a requirement of at least five samples within the averaging period. The magnitude of σ_C indicates the degree to which fluctuations in the solar wind plasma are predominantly (unidirectional) Alfvén waves.

Figure 6a shows the probability density of $|\sigma_C|$ averaged over the ahead, behind, and inverted HMF intervals. For context, 8-hour means (the average inverted HMF duration) of σ_C over the whole dataset are also shown. The plasma within the inverted HMF at 1 AU does not display particularly Alfvénic characteristics. We also consider whether the magnetic field and velocity fluctuations at the inverted HMF boundaries are correlated. Because of the averaging window used in defining contiguous inverted HMF intervals, automated determination of the precise leading and trailing boundaries in high-time resolution data is difficult (and the large number of events considered makes manual identification prohibitive). Thus we consider the maximum value of $|\sigma_C|$ in a 1-hour window centred on the identified leading and trailing boundaries. This is shown in Figure 6b. While both leading and trailing boundaries do show strong Alfvénic signatures, this association is weaker than expected by chance, as shown by the equivalent analysis for random solar wind intervals. Thus with the analysis presented here, we cannot conclude that the inverted HMF boundaries are more Alfvénic than the solar wind in general. More detailed analysis of a subset of these events will be considered in a future study. We also note that Stansby *et al.* (2019) showed that slow solar wind which is highly Alfvénic close to the Sun likely loses such signatures by 1 AU.

The time variations associated with inverted HMF are now investigated in more detail. Figure 7 shows a superposed epoch (also called a "Chree" Chree and Stagg (1928) or "composite") analysis of all 390 inverted HMF intervals, along with the solar wind for 2 days before the start of inverted HMF and 2 days after the inverted HMF trailing edge. As the duration of inverted HMF intervals is variable (between 6 and 48 hours), the duration of each interval is normalised for each event by linearly scaling and interpolating the time series. At each time point, we compute the median and one standard error.

We first consider the evolving or dynamic solar wind properties shown on the left-hand panels of Figure 7. Of the 390 inverted HMF intervals, 185 have positive radial HMF, B_R, averaged across the inverted HMF duration, $\langle B_R \rangle_{\mathrm{INV}}$. Conversely, 205 inverted HMF intervals have negative $\langle B_R \rangle_{\mathrm{INV}}$. In order to visualise the HMF polarity in the ambient solar wind
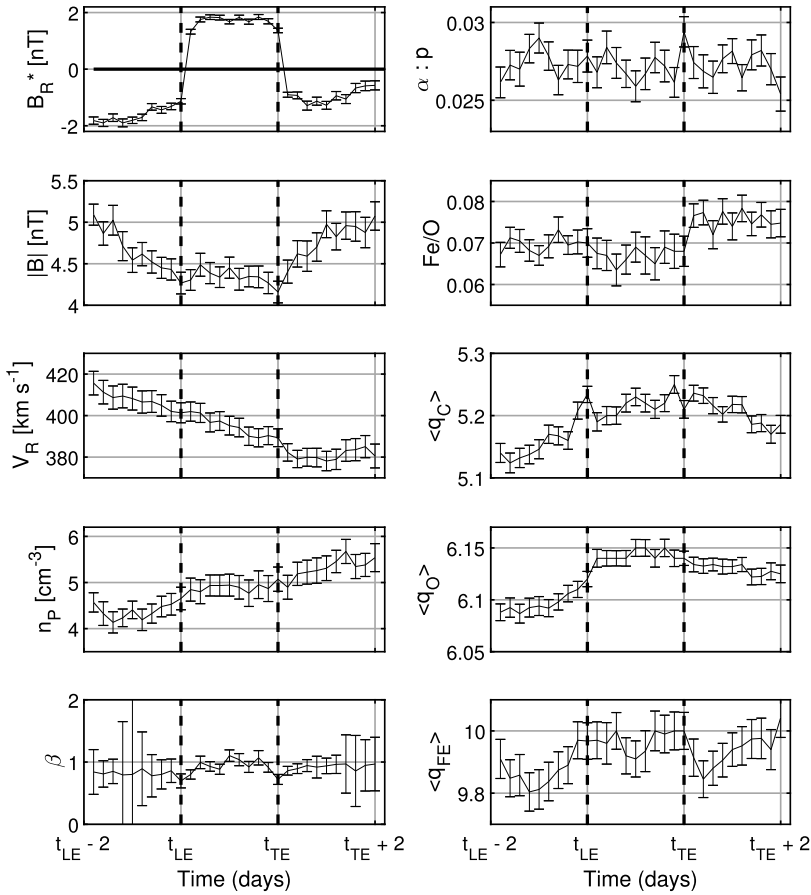
Figure 7 Superposed epoch (or "composite") analysis of all 390 inverted HMF intervals. The black line shows the median across all events and the error bars are one standard error. Vertical dashed lines show the times of the leading (t_{LE}) and trailing edges (t_{TE}) of the inverted HMF intervals, scaled to give uniform interval duration. The plots span 2 days ahead to 2 days behind the inverted HMF interval. Left-hand panels show evolving solar wind parameters of, from top to bottom: the radial HMF component (with polarity flipped where $\langle B_R \rangle < 0$ within the inverted HMF interval), HMF intensity, radial solar wind speed, proton density and plasma β. Right-hand panels show non-evolving solar wind parameters of, from top to bottom, the alpha-to-proton abundance ratio, the iron-to-oxygen abundance ratio, and average carbon, oxygen, and iron charge states.

relative to that of inverted HMF intervals, we show $B_R^* = B_R \, \mathrm{sign}(\langle B_R \rangle_{\mathrm{INV}})$. On average, inverted HMF intervals are of the opposite HMF polarity to the solar wind immediately ahead and behind, consistent with an inversion within a single magnetic sector. On average, HMF intensity within the inverted HMF intervals is lower than in the surrounding solar wind, which contributes to higher plasma β (the ratio of plasma to magnetic pressure). The inverted HMF intervals generally occur within slow radial solar wind (approximately $400\ \mathrm{km\,s^{-1}}$ at 1 AU), but the solar wind ahead is faster and less dense than that behind, with the inverted HMF intervals taking intermediate values. Solar wind density within the inverted HMF shows a flat profile, with approximately step changes from the solar wind
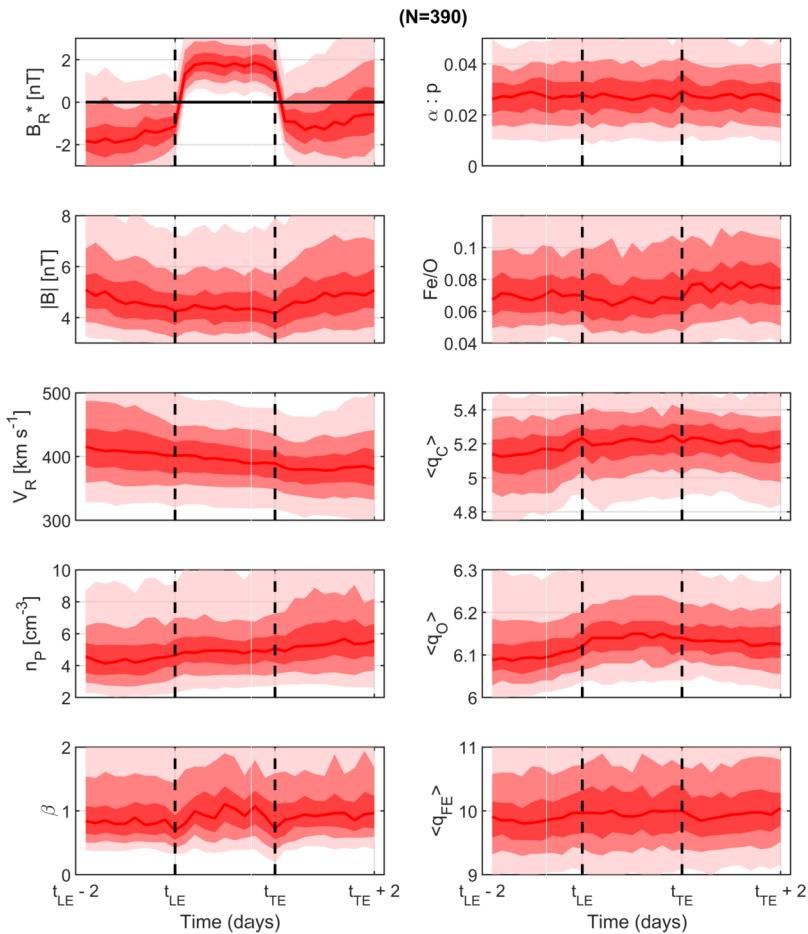
Figure 8 Same as Figure 7, but error bars show the width of the distributions to highlight the large event-to-event variability. The red line shows the median, as in Figure 7. Dark to light pink shaded regions span 25%, 50%, and 75% of the distribution, respectively.

ahead and behind. Solar wind speed declines approximately linearly through the solar wind ahead and inside the inverted HMF, and plateaus in the solar wind behind.

The right-hand panels of Figure 7 show the non-evolving solar wind parameters that are expected to be more indicative of the coronal source conditions and relatively unchanged by dynamical processes (Geiss, Gloeckler, and von Steiger, 1995; von Steiger *et al.*, 2000). The average carbon, oxygen, and iron ion charge states are proxies for coronal source temperature. Carbon and oxygen charge states suggest that the wind ahead of inverted HMF originates from cooler coronal source regions than the wind behind. This is in agreement with the speed and density signatures of fast (coronal hole) and slow (streamer belt) wind, respectively. Similarly, the iron-to-oxygen abundance ratio is lower in the solar wind ahead of an inverted HMF than in the solar wind behind, consistent with a transition from plasma of predominantly coronal hole to streamer belt composition. The alpha-to-proton abundance ratio, however, shows no consistent variation.

The inverted HMF interval has carbon and oxygen charge states in closer agreement with the slower wind behind than the faster wind ahead. Conversely, the iron-to-oxygen abundance ratio is in better agreement with the faster wind ahead.

Figure 8 shows the same data, but error bars indicate the width of the distributions. This highlights the fact that the event-to-event variability is large compared with the systematic trends in the "average" event discussed above. Thus it is important to quantitatively establish the significance of the reported trends. To do this, we compute the solar wind properties averaged over the ahead, inverted, and behind solar wind intervals. Because of the large event-to-event variability, we consider the changes in these average properties between the three intervals, rather than the properties themselves. The distributions of these changes in properties are shown as the black lines in Figure 9.

In order for these changes in average properties to be significant, the observed distribution must differ from that expected by random chance. The expected distribution by chance is computed using a Monte Carlo sampling of the data. Specifically, we select 390 random times (the number of inverted HMF intervals considered in this study) across the whole 1998–2011 period. For each random time, we compute the average properties over the 2 days ahead, for 8.3 hours immediately after the random time (as this is the median observed inverted HMF duration), and for 2 days after this period. This process is repeated 1000 times and the median of the resulting distributions shown as the red lines in Figure 9. The dark- and light-shaded pinks areas span the 33–66% and 5–95% ranges of the distributions, respectively. Thus for any given value of, e.g. $\langle V_{\mathrm{AHEAD}} \rangle - \langle V_{\mathrm{BEHIND}} \rangle$, there is a 10% chance that the observed distribution will be outside the pink uncertainty band just by chance. But this still only provides information about one specific part of the distribution and does not tell us whether the whole of the observed distribution could have occurred by chance. To assess that, all 390,000 random samples of the data are combined to produce a single random distribution which is then compared with the observed distribution. The Kolmogorov–Smirnov (KS) non-parameteric test is used to determine the probability, p, of the null hypothesis that the two distributions are subsamples of the same underlying distribution.

The black line in the top-left panel of Figure 9 shows the distribution of changes in the average value of B_R^* between the solar wind ahead and behind inverted HMF regions. It is centred on zero change and approximately symmetric. More importantly, it is indistinguishable from the pink distributions obtained by randomly sampling the time series. In this case there is a $p = 0.814$ chance that the null hypothesis explains the observed distribution, so we conclude the most likely explanation for the changes in average B_R^* between the solar wind ahead and behind inverted HMF regions is random chance, i.e. there is no significant change resulting from selecting inverted HMF intervals. Conversely, the change in average B_R^* between the ahead and inverted HMF values (as well as between the inverted HMF and behind values) can clearly not be explained by random chance. Thus inverted HMF regions are significantly associated with a B_R polarity change relative to both the solar wind ahead and behind. This particular result was already obvious from the superposed epoch analysis presented in Figure 8. But some of the following results are less obvious from the time series alone.

The HMF intensity shows the same pattern as B_R^*, with changes across the leading and trailing inverted HMF boundaries, but no significant change between the solar wind ahead and behind. The radial solar wind speed (V_R) results, shown in the third column, are particularly interesting. For the difference between the ahead and behind solar wind, the peak of the distribution is skewed towards positive values. This is suggestive of inverted HMF regions being preferentially associated with declining V_R intervals. But the randomly sampled solar wind intervals also show the same tendency. This is because the nature of solar
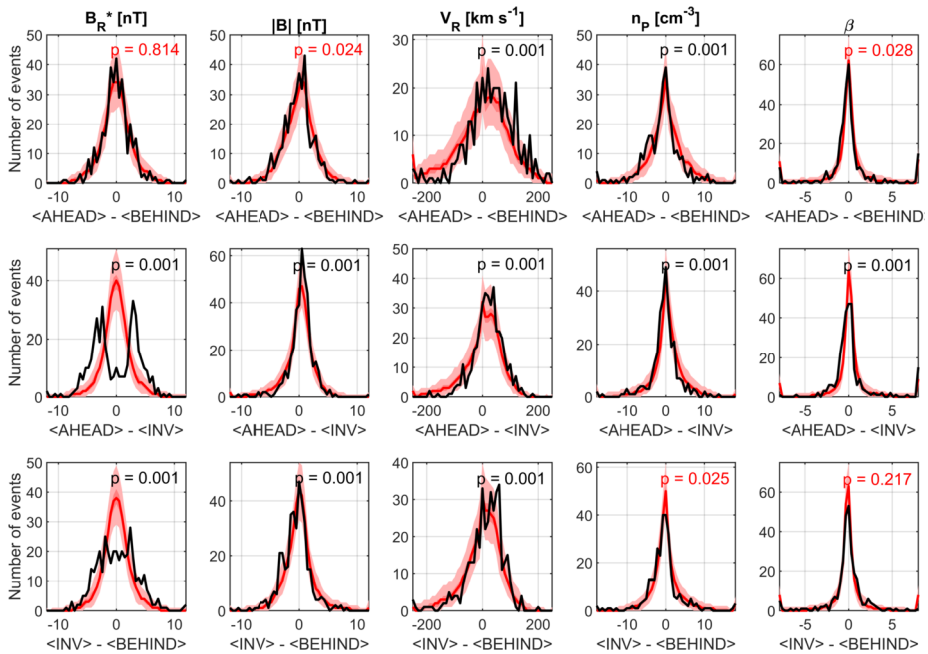
Figure 9 Changes in average solar wind properties associated with inverted HMF intervals. The black lines show histograms of the difference in average solar wind properties ahead and behind ($\langle AHEAD \rangle - \langle BEHIND \rangle$, top row), ahead and within ($\langle AHEAD \rangle - \langle INV \rangle$, middle row), and within and behind ($\langle INV \rangle - \langle BEHIND \rangle$, bottom row) inverted HMF intervals. Red lines show the equivalent changes for random solar wind intervals, with light and dark pink regions showing 1-sigma and 95% uncertainty intervals. Probabilities (p) that the observed and randomly sampled distributions are drawn from the same underlying distribution are shown. Columns, from left to right, show the radial HMF component (with polarity flipped when $\langle B_R \rangle$ is less than 0 within the inverted HMF interval), HMF intensity, radial solar wind speed, proton density and plasma β.

wind stream interactions means that the V_R time series often exhibits a saw-tooth profile, with a sharp rise followed by a gradual decline over a period of a few days (e.g. Gosling and Pizzo, 1999). Thus the difference in solar wind speed approximately one day either side of a randomly selected time is more likely to show a decrease in V_R than it is to show an increase. However, the KS test suggests the observed change in V_R is greater than that expected by chance. This is also true for the change in average V_R from ahead to inverted, and from inverted to behind intervals. Proton density is significantly lower ahead of the inverted HMF than behind. Density changes across the leading inverted HMF boundary, but not the trailing boundary. This is consistent with fast, tenuous wind ahead of the inverted HMF, but slow, dense wind in the inverted HMF interval and behind. The plasma β shows a change from the ahead solar wind to the inverted HMF, but not from the inverted HMF to the behind solar wind. Again, consistent with the inverted HMF being more like the slow wind behind.

Figure 10 shows the same analysis for the ion properties. As expected from the time series plots, there are no significant changes in the average alpha-to-proton abundance ratios associated with inverted HMF. Alpha-to-proton abundance ratio is known to be a function of solar wind speed (Borrini *et al.*, 1983; Kasper *et al.*, 2007) and so a trend might be expected, but any variation must be too weak relative to the natural variability to be revealed by the present analysis. However, the other available measure of elemental composition, the iron-to-oxygen ion abundance ratio (Fe/O), does show significant differences. The solar wind
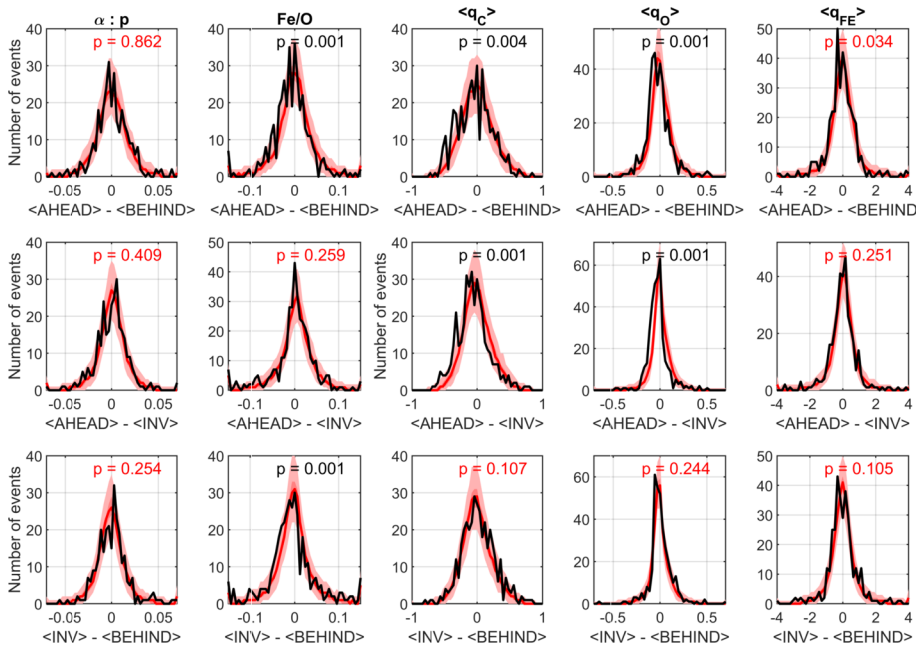
Figure 10 Changes in ion properties around inverted HMF intervals in the same format as Figure 9. Columns, from left to right, show changes in the alpha-to-proton abundance ratio, the iron-to-oxygen abundance ratio, and average charge states of carbon, oxygen, and iron.

ahead shows significantly lower Fe/O than the solar wind behind, as expected for coronal hole and streamer belt sources, respectively (Zurbuchen, 2007). Fe/O in the inverted HMF is significantly lower than in the slower wind behind, but is essentially the same as the faster wind ahead. For carbon and oxygen ion charge average states, the solar wind behind HMF inversions is significantly elevated relative to that ahead, as expected (Fu *et al.*, 2017). Unlike the Fe/O, oxygen and carbon charge states in inverted HMF intervals are indistinguishable from the slower wind behind and significantly different from the faster wind ahead. For the average iron charge state, there are no significant changes.

4. Discussion

In this study, we have investigated the possibility of observing coronal loop opening signatures in the solar wind at 1 AU. In the first part of the paper, simple scaling arguments were used to illustrate that inversions generated in the corona as a direct result of interchange reconnection are unlikely to survive to 1 AU without the addition of a dynamical process, such as solar wind speed shear. This is in broad agreement with previous numerical MHD results (Landi, Hellinger, and Velli, 2005, 2006). However, as pointed out by Owens *et al.* (2018), for a newly-opened coronal loop, the initial sense of the associated solar wind stream shear produced directly by loop opening is likely to further contribute to the destruction of inverted HMF, rather than maintain it. Instead, it was proposed that inversions form as a result of stream shear formed later when the footpoint of the newly opened coronal loop (and source of slow wind) convects deeper into a coronal hole and becomes a source of fast

wind. In this scenario, the speed shear should be in opposition to the magnetic curvature force. Thus the relative radial variation of these two effects controls inverted HMF formation and destruction. The Alfvén speed, and hence the ability to reduce HMF inversions, rapidly decreases with heliocentric distance (Figure 1). The solar wind shear will decay due to momentum exchange resulting from the interaction of fast and slow solar wind streams, but this is likely to be a slower fall off than that of Alfvén speed. Thus once the Alfvén speed has dropped sufficiently, inverted HMF intervals will begin to grow with heliocentric distance while the speed shear is present, after which they will again begin to decay at the local Alfvén speed.

The second part of the study examined in situ observations of inverted HMF at 1 AU, particularly with respect to the surrounding solar wind. Using an automated algorithm, 390 inverted HMF intervals were selected, with a median duration of around 8 hours. Thus these structures are much larger than the sub-minute HMF inversions identified in the inner heliosphere by Horbury, Matteini, and Stansby (2018), which are not thought to survive to 1 AU. The larger inverted HMF regions that we identify at 1 AU do not show significant Alfvénic signatures. They are found to be in approximate pressure balance with the solar wind behind, but not ahead.

Inverted HMF intervals preferentially occur in declining solar wind speed regions. However, the shear is relatively weak and the characteristic pattern of fast-slow-fast solar wind predicted by Owens *et al.* (2018) is not obvious. It is possible that this signature fails to survive to 1 AU owing to stream interaction, or that the a stationary spacecraft at 1 AU does not typically cut through the complete solar wind structure. Inner heliosphere observations may shed light on this issue. Ion composition and charge-state measurements support the idea that inverted HMF occurs at the transition from coronal hole to streamer belt wind. Inverted HMF was initially identified in conjunction with the heliospheric current sheet, and therefore a reversal in the polarity of radial magnetic field (Crooker *et al.*, 2004; Crooker and McPherron, 2012). However, we here show that large HMF inversions are primarily embedded within unipolar HMF regions, with a temporary reversal in the magnetic field polarity only within the inversion itself.

Within HMF inversions, the magnetic field intensity is significantly depressed relative to the surrounding solar wind, while the density and speed are intermediate between the tenuous, fast wind ahead and the dense, slow wind behind. Thus inverted HMF tends to be higher plasma beta than the fast wind ahead, but comparable to the slow wind behind. Similarly, the oxygen and carbon charge states within inverted HMF are in agreement with slow solar wind and preferential heating in the low corona (Gruesbeck *et al.*, 2011). Iron charge states are generally thought to be elevated by extended heating through the corona (Lepri *et al.*, 2012; Song *et al.*, 2016) and have been found to be more variable within otherwise like-composition streams (Heidrich-Meisner *et al.*, 2016). We find that iron charge states exhibit the greatest degree of event-to-event variability and show no significant variations in the vicinity of inverted HMF. Ion composition variations within inverted HMF show low iron-to-oxygen abundances, in closer agreement with the fast wind ahead than the slow wind behind. Alpha abundance shows no significant variation about inverted HMF.

Thus inverted HMF at 1 AU is associated with preferential heating in the low corona, greater than that expected in coronal holes, and low abundance of first-ionisation potential (FIP) elements, closer to that expected of coronal holes (Feldman and Widing, 2003). Recent spectroscopic measurements of the quiet Sun suggest it has approximately photospheric composition, while active regions have enhanced abundances of low first-ionisation potential elements, such as iron (Del Zanna, 2019). Thus the observations presented here are more consistent with large-scale inverted HMF forming via opening of small-scale quiet

sun loops, rather than large-scale active region loops with high FIP abundance. It should be noted, however, that in order to generate the inversion via solar wind speed shear in the heliosphere, the solar wind source on the same flux tube must vary with time. Mixing of plasma populations has recently been invoked to explain remote spectroscopic observations (Laming *et al.*, 2019). It could result in more complex ion signatures than the simple picture presented here, particularly with differential streaming of ion populations (Macneil, 2019; Schwadron *et al.*, 2005; Berger, Wimmer-Schweingruber, and Gloeckler, 2011). Indirect evidence of multiple plasma sources may be present through the existence of ion cyclotron waves (Wicks *et al.*, 2016) or torsional Alfvén waves (Higginson and Lynch, 2018).

Disclosure of Potential Conflicts of Interest   We declare we have no conflicts of interest.

Publisher's Note   Springer Nature remains neutral with regard to jurisdictional claims in published maps and institutional affiliations.

References

Antiochos, S.K., Mikic, Z., Titov, V.S., Lionello, R., Linker, J.A.: 2011, A model for the sources of the slow solar wind. *Astrophys. J.* **731**, 112. DOI.

Baker, D., Rouillard, A.P., van Driel-Gesztelyi, L., Démoulin, P., Harra, L.K., Lavraud, B., Davies, J.A., Opitz, A., Luhmann, J.G., Sauvaud, J.-A., Galvin, A.B.: 2009, Signatures of interchange reconnection: STEREO, ACE and Hinode observations combined. *Ann. Geophys.* **27**(10), 3883. DOI.

Balogh, A., Forsyth, R.J., Lucek, E.A., Horbury, T.S., Smith, E.J.: 1999, Heliospheric magnetic field polarity inversions at high heliographic latitudes. *Geophys. Res. Lett.* **26**, 631. DOI.

Berger, L., Wimmer-Schweingruber, R.F., Gloeckler, G.: 2011, Systematic measurements of ion-proton differential streaming in the solar wind. *Phys. Rev. Lett.* **106**(15), 151103. DOI.

Borrini, G., Gosling, J.T., Bame, S.J., Feldman, W.C.: 1983, Helium abundance variations in the solar wind. *Solar Phys.* **83**(2), 367. DOI.

Bruno, R., Carbone, V.: 2005, The solar wind as a turbulence laboratory. *Living Rev. Solar Phys.* **2**, 4. DOI.

Chree, C., Stagg, J.M.: 1928, Recurrence phenomena in terrestrial magnetism. *Phil. Trans. Roy. Soc., Math. Phys. Eng. Sci.* **227**, 21. DOI.

Cranmer, S.R., Ballegooijen, A.A.v., Edgar, R.J.: 2007, Self-consistent coronal heating and solar wind acceleration from anisotropic magnetohydrodynamic turbulence. *Astrophys. J. Suppl.* **171**(2), 520. DOI.

Crooker, N.U., McPherron, R.L.: 2012, Coincidence of composition and speed boundaries of the slow solar wind. *J. Geophys. Res.* **117**(A9), A09104. DOI.

Crooker, N.U., Owens, M.J.: 2011, Interchange reconnection: remote sensing of solar signature and role in heliospheric magnetic flux budget. *Space Sci. Rev.* **172**(1–4), 201. DOI.

Crooker, N.U., Kahler, S.W., Larson, D.E., Lin, R.P.: 2004, Large-scale magnetic field inversions at sector boundaries. *J. Geophys. Res.* **109**, A03108. DOI.

Del Zanna, G.: 2019, The EUV spectrum of the Sun: quiet- and active-Sun irradiances and chemical composition. *Astron. Astrophys.* **624**, A36. DOI.

Ebert, R.W., McComas, D.J., Elliott, H.A., Forsyth, R.J., Gosling, J.T.: 2009, Bulk properties of the slow and fast solar wind and interplanetary coronal mass ejections measured by Ulysses: three polar orbits of observations. *J. Geophys. Res.* **114**(A1), A01109. DOI.

Edmondson, J.K., Antiochos, S.K., DeVore, C.R., Lynch, B.J., Zurbuchen, T.H.: 2010, Interchange reconnection and coronal hole dynamics. *Astrophys. J.* **714**(1), 517. DOI.

Feldman, U., Widing, K.G.: 2003, Elemental abundances in the solar upper atmosphere derived by spectroscopic means. *Space Sci. Rev.* **107**(3/4), 665. DOI.

Fisk, L.A.: 2003, Acceleration of the solar wind as a result of the reconnection of open magnetic flux with coronal loops. *J. Geophys. Res.* **108**, 1157. DOI.

Fox, N.J., Velli, M.C., Bale, S.D., Decker, R., Driesman, A., Howard, R.A., Kasper, J.C., Kinnison, J., Kusterer, M., Lario, D., Lockwood, M.K., McComas, D.J., Raouafi, N.E., Szabo, A.: 2016, The Solar Probe Plus mission: humanitýs first visit to our star. *Space Sci. Rev.* **204**(1–4), 7. DOI.

Fu, H., Madjarska, M.S., Xia, L., Li, B., Huang, Z., Wangguan, Z.: 2017, Charge states and FIP bias of the solar wind from coronal holes, active regions, and quiet Sun. *Astrophys. J.* **836**(2), 169. DOI.

Geiss, J., Gloeckler, G., von Steiger, R.: 1995, Origin of the solar wind from composition data. *Space Sci. Rev.* **72**, 49. DOI.

Gloeckler, G., Cain, J., Ipavich, F.M., Tums, E.O., Bedini, P., Fisk, L.A., Zurbuchen, T.H., Bochsler, P., Fischer, J., Wimmer-Schweingruber, R.F.: 1998, Investigation of the composition of solar and interstellar matter using solar wind and pickup ion measurements with SWICS and SWIMS on the ACE spacecraft. *Space Sci. Rev.* **86**, 497. DOI.

Gosling, J.T., Pizzo, V.J.: 1999, Formation and evolution of corotating interaction regions and their three dimensional structure. *Space Sci. Rev.* **89**, 21. DOI.

Gosling, J.T., Baker, D.N., Bame, S.J., Feldman, W.C., Zwickl, R.D.: 1987, Bidirectional solar wind electron heat flux events. *J. Geophys. Res.* **92**, 8519. DOI.

Gruesbeck, J.R., Lepri, S.T., Zurbuchen, T.H., Antiochos, S.K.: 2011, Constraints on coronal mass ejection evolution from in situ observations of ionic charge states. *Astrophys. J.* **730**(2), 103. DOI.

Heidrich-Meisner, V., Peleikis, T., Kruse, M., Berger, L., Wimmer-Schweingruber, R.: 2016, Observations of high and low Fe charge states in individual solar wind streams with coronal-hole origin. *Astron. Astrophys.* **593**, A70. DOI.

Higginson, A.K., Lynch, B.J.: 2018, Structured slow solar wind variability: streamer-blob flux ropes and torsional Alfvén waves. *Astrophys. J.* **859**(1), 6. DOI.

Horbury, T.S., Matteini, L., Stansby, D.: 2018, Short, large-amplitude speed enhancements in the near-Sunfast solar wind. *Mon. Not. Roy. Astron. Soc.* **478**(2), 1980. DOI.

Kahler, S.W., Crooker, N.U., Gosling, J.T.: 1996, The topology of intrasector reversals of the interplanetary magnetic field. *J. Geophys. Res.* **101**, 24373. DOI.

Kasper, J.C., Stevens, M.L., Lazarus, A.J., Steinberg, J.T., Ogilvie, K.W.: 2007, Solar wind helium abundance as a function of speed and heliographic latitude: variation through a solar cycle. *Astrophys. J.* **660**(1), 901. DOI.

Kepko, L., Viall, N.M., Antiochos, S.K., Lepri, S.T., Kasper, J.C., Weberg, M.: 2016, Implications of L1 observations for slow solar wind formation by solar reconnection. *Geophys. Res. Lett.* **43**(9), 4089. DOI.

Laming, J.M., Vourlidas, A., Korendyke, C., Chua, D., Cranmer, S.R., Ko, Y.-K., Kuroda, N., Provornikova, E., Raymond, J.C., Raouafi, N.-E., Strachan, L., Tun-Beltran, S., Weberg, M., Wood, B.E.: 2019, Element abundances: A new diagnostic for the solar wind. *Astrophys. J.* **879**(2), 124. DOI.

Landi, S., Hellinger, P., Velli, M.: 2005, On the origin of the heliospheric magnetic field polarity inversion at high latitudes. In: *Solar Wind 11/SOHO 16, Connecting Sun and Heliosphere* **592**, 785.

Landi, S., Hellinger, P., Velli, M.: 2006, Heliospheric magnetic field polarity inversions driven by radial velocity field structures. *Geophys. Res. Lett.* **33**(14), L14101. DOI.

Lepri, S.T., Laming, J.M., Rakowski, C.E., Von Steiger, R.: 2012, Spatially dependent heating and ionization in an ICME observed by both ACE and Ulysses. *Astrophys. J.* **760**(2), 105. DOI.

Li, X., Habbal, S.R., Kohl, J.L., Noci, G.: 1998, The effect of temperature anisotropy on observations of Doppler dimming and pumping in the inner corona. *Astrophys. J.* **501**(1), L133. DOI.

Lockwood, M., Owens, M.J., Macneil, A.: 2019, On the origin of ortho-gardenhose heliospheric flux. *Solar Phys.* **294**(6), 85. DOI.

Lockwood, M., Owens, M.J., Rouillard, a.P.: 2009, Excess open solar magnetic flux from satellite data: 2. A survey of kinematic effects. *J. Geophys. Res.* **114**(A11), 1. DOI.

Macneil, A.R.: 2019, Solar Wind Particle Populations at 1 AU: Examining their Origins in Advance of the Doctoral thesis, UCL (University College London). http://discovery.ucl.ac.uk/10066843/.

Matteini, L., Horbury, T.S., Pantellini, F., Velli, M., Schwartz, S.J.: 2015, Ion kinetic energy conservation and magnetic field strength constancy in muli-fluid solar wind Alfvénic turbulence. *Astrophys. J.* **802**(1), 11. DOI.

McComas, D.J., Bame, S.J., Barker, S.J., Feldman, W.C., Phillips, J.L., Riley, P., Griffee, J.W.: 1998, Solar wind electron proton alpha monitor (SWEPAM) for the advanced composition explorer. *Space Sci. Rev.* **86**, 563. DOI.

McComas, D.J., Elliott, H.A., Schwadron, N.A., Gosling, J.T., Skoug, R.M., Goldstein, B.E.: 2003, The three-dimensional solar wind around solar maximum. *Geophys. Res. Lett.* **30**, 1517. DOI.

Muller, D., Marsden, R.G., St. Cyr, O.C., Gilbert, H.R., Team, T.S.O.: 2013, Solar orbiter. *Solar Phys.* **285**(1–2), 25. DOI.

Nash, A.G., Sheeley, N.R., Wang, Y.-M.: 1988, Mechanisms for the rigid rotation of coronal holes. *Solar Phys.* **117**(2), 359. DOI.

Neugebauer, M., Goldstein, B.E., McComas, D.J., Suess, S.T., Balogh, A.: 1995, Ulysses observations of microstreams in the solar wind from coronal holes. *J. Geophys. Res.* **1002**, 23389. DOI.

Newkirk, G.: 1967, Structure of the solar corona. *Annu. Rev. Astron. Astrophys.* **5**(1), 213. DOI.

Owens, M.J., Crooker, N.U.: 2007, Reconciling the electron counterstreaming and dropout occurrence rates with the heliospheric flux budget. *J. Geophys. Res.* **112**(A6), 1. DOI.

Owens, M.J., Crooker, N.U., Lockwood, M.: 2013, Solar origin of heliospheric magnetic field inversions: evidence for coronal loop opening within pseudostreamers. *J. Geophys. Res.* **118**, 1868. DOI.

Owens, M.J., Crooker, N.U., Lockwood, M.: 2014, Solar cycle evolution of dipolar and pseudostreamer belts and their relation to the slow solar wind. *J. Geophys. Res.* **119**, 36. DOI.

Owens, M.J., Lockwood, M., Riley, P., Linker, J.: 2017, Sunward strahl: A method to unambiguously determine open solar flux from in situ spacecraft measurements using suprathermal electron data. *J. Geophys. Res.* **122**(11), 910. DOI.

Owens, M.J., Lockwood, M., Barnard, L.A., MacNeil, A.R.: 2018, Generation of inverted heliospheric magnetic flux by coronal loop opening and slow solar wind release. *Astrophys. J.* **868**(1), L14. DOI.

Parker, E.N.: 1958, Dynamics of the interplanetary gas and magnetic fields. *Astrophys. J.* **128**, 664. DOI.

Pilipp, W.G., Muehlhaeuser, K.-H., Miggenrieder, H., Rosenbauer, H., Schwenn, R.: 1987, Variations of electron distribution functions in the solar wind. *J. Geophys. Res.* **92**, 1103. DOI.

Riley, P., Gosling, J.T., Crooker, N.U.: 2004, Ulysses observations of the magnetic connectivity between coronal mass ejections and the Sun. *Astrophys. J.* **608**, 1100. DOI.

Schatten, K.H., Wilcox, J.M., Ness, N.F.: 1969, A model of interplanetary and coronal magnetic fields. *Solar Phys.* **9**, 442. DOI.

Schwadron, N.A., McComas, D.J., Elliott, H.A., Gloeckler, G., Geiss, J., von Steiger, R.: 2005, Solar wind from the coronal hole boundaries. *J. Geophys. Res.* **110**(A4), A04104. DOI.

Sheeley, N.R. Jr., Wang, Y.â, Hawley, S.H., Brueckner, G.E., Dere, K.P., Howard, R.A., Koomen, M.J., Korendyke, C.M., Michels, D.J., Paswaters, S.E., Socker, D.G., St. Cyr, O.C., Wang, D., Lamy, P.L., Llebaria, A., Schwenn, R., Simnett, G.M., Plunkett, S., Biesecker, D.A.: 1997, Measurements of flow speeds in the corona between 2 and 30 R. *Astrophys. J.* **484**(1), 472. DOI.

Shodhan, S., Crooker, N.U., Kahler, S.W., Fitzenreiter, R.J., Larson, D.E., Lepping, R.P., Siscoe, G.L., Gosling, J.T.: 2000, Counterstreaming electrons in magnetic clouds. *J. Geophys. Res.* **105**, 27261. DOI.

Smith, C.W., L'Heureux, J., Ness, N.F., Acuna, M.H., Burlaga, L.F., Scheifele, J.: 1998, The ACE magnetic fields experiment. *Space Sci. Rev.* **86**, 613. DOI.

Song, H.Q., Zhong, Z., Chen, Y., Zhang, J., Cheng, X., Zhao, L., Hu, Q., Li, G.: 2016, A statistical study of the average iron charge state distributions inside magnetic clouds for solar cycle 23. *Astrophys. J. Suppl.* **224**(2), 27. DOI.

Stansby, D., Horbury, T.S., Matteini, L.: 2019, Diagnosing solar wind origins using in situ measurements in the inner heliosphere. *Mon. Not. Roy. Astron. Soc.* **482**(2), 1706. DOI.

Stansby, D., Matteini, L., Horbury, T.S., Perrone, D., D'Amicis, R., Beri, L.: 2019, The origin of slow Alfvénic solar wind at solar minimum. arXiv.

Velli, M., Lionello, R., Linker, J.A., Mikic, Z.: 2011, Coronal plumes in the fast solar wind. *Astrophys. J.* **736**(1), 32. DOI.

Viall, N.M., Spence, H.E., Kasper, J.: 2009, Are periodic solar wind number density structures formed in the solar corona? *Geophys. Res. Lett.* **36**, 23102. DOI.

von Steiger, R., Schwadron, N.A., Fisk, L.A., Geiss, J., Gloeckler, G., Hefti, S., Wilken, B., Wimmer–Schweingruber, R.R., Zurbuchen, T.H.: 2000, Composition of quasi–stationary solar wind flows from Ulysses/Solar Wind Ion Composition Spectrometer. *J. Geophys. Res.* **105**(A12), 27217. DOI.

Wang, Y.-M., Sheeley, N.R. Jr.: 1990, Solar wind speed and coronal flux-tube expansion. *Astrophys. J.* **355**, 726. DOI.

Wicks, R.T., Alexander, R.L., Stevens, M., Wilson, L.B. III, Moya, P.S., Viñas, A., Jian, L.K., Roberts, D.A., O'Modhrain, S., Gilbert, J.A., Zurbuchen, T.H.: 2016, A proton-cyclotron wave storm generated by unstable proton distribution functions in the solar wind. *Astrophys. J.* **819**(1), 6. DOI.

Yamauchi, Y., Suess, S.T., Steinberg, J.T., Sakurai, T.: 2004, Differential velocity between solar wind protons and alpha particles in pressure balance structures. *J. Geophys. Res.* **109**(A3), A03104. DOI.

Zurbuchen, T.H.: 2007, A new view of the coupling of the Sun and the heliosphere. *Annu. Rev. Astron. Astrophys.* **45**, 297. DOI.